Serial crystallography captures dynamic control of sequential electron and proton transfer events in a flavoenzyme

Manuel Maestre-Reyna, Cheng-Han Yang, Eriko Nango, Wei-Cheng Huang, Eka Putra Gusti Ngurah Putu, Wen-Jin Wu, Po-Hsun Wang, Sophie Franz-Badur, Martin Saft, Hans-Joachim Emmerich, et al.

Serial crystallography captures dynamic control of sequential electron and proton transfer events in a flavoenzyme

Manuel Maestre-Reyna[1], Cheng-Han Yang[1], Eriko Nango[2,3], Wei-Cheng Huang[1], Eka Putra Gusti Ngurah Putu[1], Wen-Jin Wu[1], Po-Hsun Wang[1], Sophie Franz-Badur[4], Martin Saft[4], Hans-Joachim Emmerich[4], Hsiang-Yi Wu[1], Cheng-Chung Lee[1], Kai-Fa Huang[1], Yao-Kai Chang[1], Jiahn-Haur Liao[1], Jui-Hung Weng[1], Wael Gad[1], Chiung-Wen Chang[1], Allan H. Pang[1], Michihiro Sugahara[2], Shigeki Owada[5], Yuhei Hosokawa[6], Yasumasa Joti[2,5], Ayumi Yamashita[2,3], Rie Tanaka[2,3], Tomoyuki Tanaka[2,3], Luo Fangjia[2,3], Kensuke Tono[5], Kai-Cheng Hsu[7], Stephan Kiontke[4], Igor Schapiro[8], Roberta Spadacini[9], Antoine Royant[10,11], Junpei Yamamoto[6], So Iwata[2,3], Lars-Oliver Essen[4,12,*], Yoshitaka Bessho[1,2,*], Ming-Daw Tsai[1,13,*]

Affiliations:

[1]Institute of Biological Chemistry, Academia Sinica, 128 Academia Rd. Sec. 2, Nankang, Taipei, 115, Taiwan.

[2]RIKEN SPring-8 Center, 1-1-1 Kouto, Sayo, Hyogo, 679-5148, Japan.

[3]Department of Cell Biology, Graduate School of Medicine, Kyoto University, Yoshidakonoe-cho, Sakyo-ku, Kyoto, 606-8501, Japan.

[4]Department of Chemistry, Philipps University Marburg, Hans-Meerwein Strasse 4, Marburg 35032, Germany.

[5]Japan Synchrotron Radiation Research Institute, 1-1-1 Kouto, Sayo, Hyogo, 679-5198, Japan.

[6]Division of Chemistry, Graduate School of Engineering Science, Osaka University, 1-3 Machikaneyama, Toyonaka, Osaka 560-8531, Japan.

[7]Graduate Institute of Cancer Biology and Drug Discovery, College of Medical Science and Technology, Taipei Medical University, Taipei, Taiwan

[8]Fritz Haber Center for Molecular Dynamics, Institute of Chemistry
The Hebrew University of Jerusalem, Jerusalem 91904, Israel

[9]Dipartamento di Scienze e tecnologie, Universita degli studi del Sannio, Benevento, Italy.

[10]Institut de Biologie Structurale (IBS), University Grenoble Alpes, CNRS, CEA, 38044 Grenoble, France.

[11]European Synchrotron Radiation Facility, 38043 Grenoble, France.

[12]Center of Synthetic Microbiology, Philipps University Marburg, Hans-Meerwein Straße 4, 35032 Marburg, Germany.

[13]Institute of Biochemical Sciences, National Taiwan University, 1, Roosevelt Rd. Sec. 4, Taipei 106, Taiwan.

***e-mail:** mdtsai@gate.sinica.edu.tw ; bessho@sinica.edu.tw ; essen@chemie.uni-marburg.de

Abstract

Flavin coenzymes are universally found in biological redox reactions. DNA photolyases with their flavin chromophore (FAD) utilize blue light for DNA repair and photoreduction. The latter process involves two single-electron transfers to FAD with an intermittent protonation step to prime the enzyme active for DNA repair. Here we use time-resolved serial femtosecond X-ray crystallography to describe how light-driven electron transfers trigger subsequent nanosecond-to-microsecond entanglement between FAD and its Asn/Arg-Asp redox sensor triad. We found that this key feature within the photolyase-cryptochrome family regulates FAD re-hybridization and protonation. After first electron transfer, the $FAD^{\bullet-}$ isoalloxazine ring twists strongly when the arginine closes in to stabilize the negative charge. Subsequent breakage of the arginine-aspartate salt bridge promotes proton transfer from arginine to $FAD^{\bullet-}$. Our molecular movies demonstrate how the protein environment of redox cofactors organizes multiple electron/proton transfer events in an ordered fashion, which could be applicable to other redox systems such as photosynthesis.

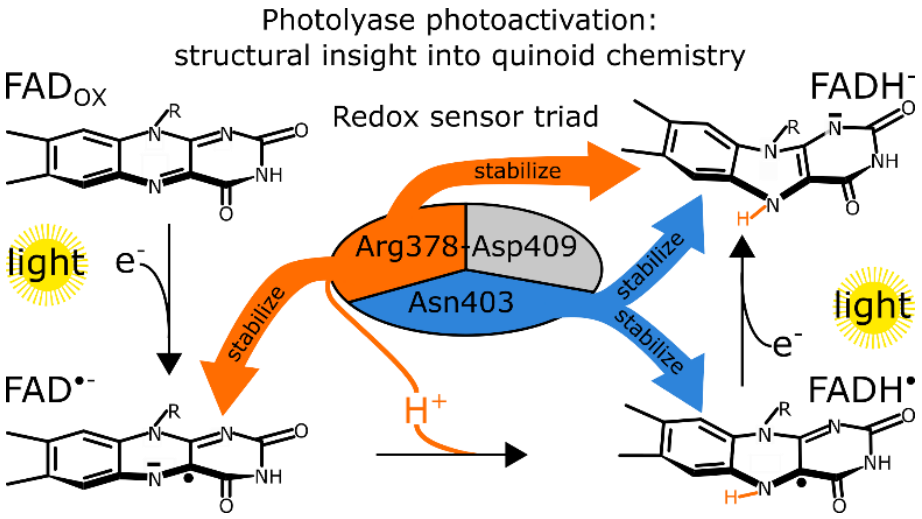

All biological systems depend on electron transport chains (ETCs) to fuel their metabolism, most commonly in the form of photosynthesis and respiration[1,2]. Although ETC proteins, such as cytochromes and iron-sulphur proteins[3], can only transfer single electrons, ETC catalyzed reaction cycles always result in the net flow of two electrons from donor to acceptor[4]. This apparent paradox is solved by quinoid molecules such as membrane-resident quinones used by photosynthetic reaction centres and respiratory chains as substrates or enzyme-bound flavin adenine dinucleotide (FAD) and flavin mononucleotide (FMN) cofactors [5]. These molecules can capture either one or two electrons and exist hence in three possible redox states: oxidized (quinone), radical semi-reduced (semiquinone) or fully reduced (hydroquinone)[6]. One particularly interesting example for multiple electron transfer (ET) reactions on FAD is the photoreduction of DNA photolyases, a process by which this ubiquitous class of DNA repair flavoenzymes reduces their FAD coenzyme to the catalytically active $FADH^-$ state[7]. Here, two light-driven, sub-nanosecond, single ET events transform inactive FAD_{ox} into the hydroquinoid $FADH^-$ via two long-lived radical semiquinone intermediates, $FAD^{\bullet-}$ and its subsequently protonated form $FADH^\bullet$ (Fig. 1a)[8]. The ETC fuelling these reactions consists mostly of a tryptophan triad (Fig 1b)[9,10], or less frequently a tetrad[11], which ultimately extracts an electron from the environment[12]. In the photoactivated state, DNA photolyases finally catalyse blue light-driven DNA repair of UV photolesions such as cyclobutane pyrimidine dimers (CPD)[13] (Fig. 1c) by injecting an electron from excited $FADH^{-*}$ onto the DNA lesion and transient formation of semi-reduced $FADH^\bullet$[14].

Over the last three decades, the flavin redox chemistry of photolyases has been extensively characterized via spectroscopic and theoretical studies at ps-ns (reduction) and µs-ms (re-oxidation) time-scales[10,12,15–19]. However, information on the stabilization of the post-electron transfer flavin species (ns-µs) by their surrounding protein matrix, which has been hypothesized to enable quinoid chemistry[8,20], is lacking. Furthermore, spectroscopic

characterization was mostly restricted to electronic transitions of the flavin species and the ETC, providing very little information regarding flavin geometry and thereby induced protein conformational changes[8,10,12,16,21]. In addition, flavin radical intermediates are too short-lived for conventional crystallographic analysis, and the structures of flavoenzymes often suffer from radiation-damage due to X-ray mediated flavin reduction[22–25]. Conversely, the recent development of X-ray free electron laser (XFEL) facilities in combination with serial femtosecond crystallography (SFX) techniques[26] has allowed for damage-free data collection of biologically relevant macromolecular structures[27,28], particularly under time-resolved conditions (TR-SFX) at ultrashort intervals[22,29–36].

In this study, we structurally characterize FAD redox- and post-electron transfer changes in the nanosecond to millisecond range, and analyze how each intermediate species is stabilized, as they occur in the *Methanosarcina mazei* class II DNA photolyase (*Mm*CPDII)[23] via TR-SFX. By analyzing a total of 23 structures, we were able to determine the redox- and time-dependent structural changes in the FAD coenzyme elicited by the sub-nanosecond photoreduction events, elucidate the mechanism of $FAD^{\bullet-}$ protonation, and uncover an FAD redox sensor triad Asn/Arg-Asp that differentially stabilizes each flavin redox species, thus providing unprecedented insight into the structural mechanics of quinoid-protein chemistry.

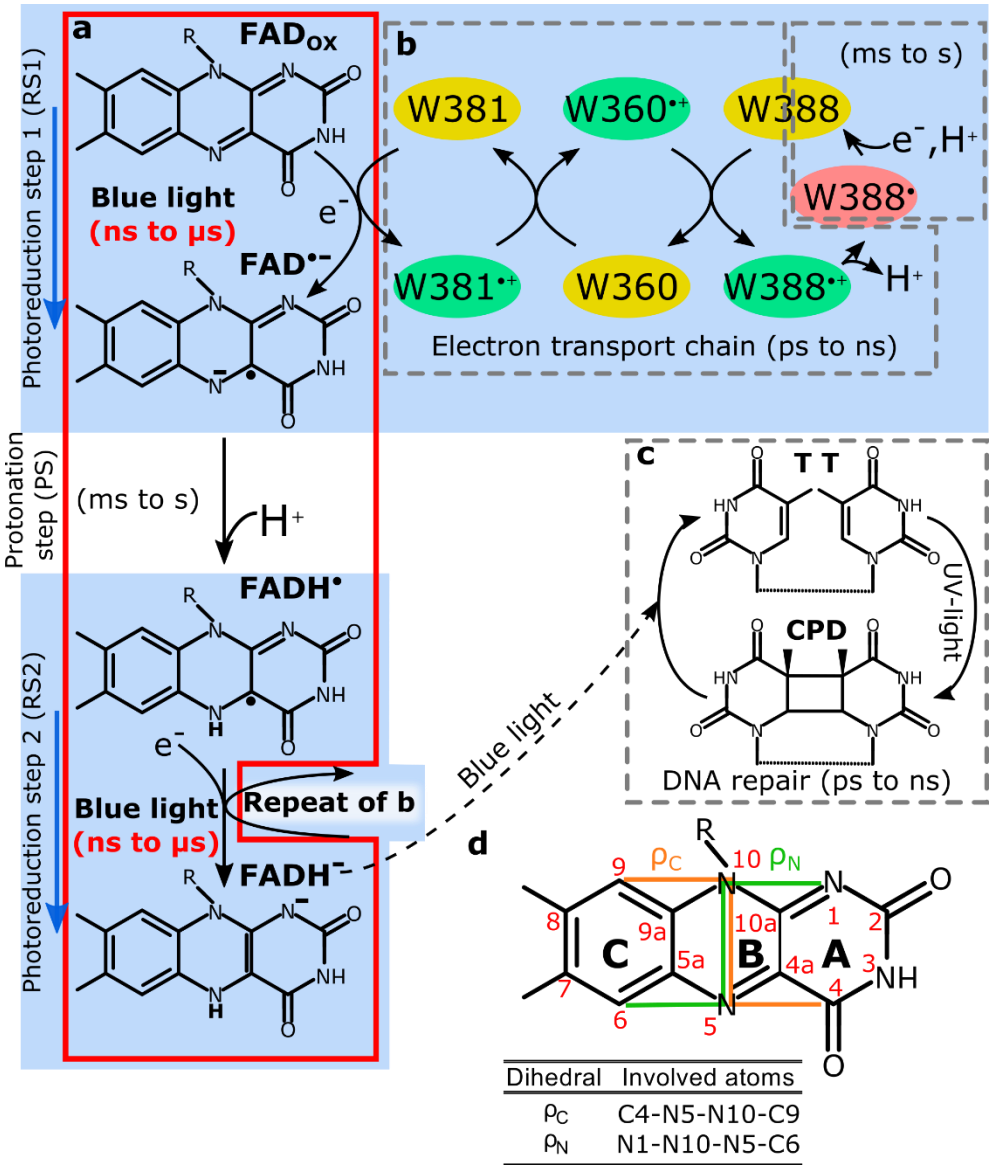

Figure. 1. Reactions catalyzed by DNA photolyases. (**a**) During photoactivation, two photoreduction steps (RS1 and RS2, shaded blue) sequentially inject one electron each into FAD, reducing FAD_{ox} to $FADH^-$. (**b**) Each photoreduction step involves a tryptophan triad (W381-W360-W388 in *Mm*CPDII), which acts as an electron transport chain. (**c**) Light-triggered repair of UV-damaged DNA containing a CPD. The time ranges marked in red in (a) were determined in this study, while all other timings are adapted from literature. (**d**) Isoalloxazine ring structure with definition of dihedral angles ρ_C (orange) and ρ_N (green).

99

Results

Experimental approach and overall nomenclature

In photolyases, and in the absence of an external reducing agent, photoreduction stalls at the end of photoreduction step 1 (RS1), unable to proceed to photoreduction step 2 (RS2) without prior protonation of the anionic semiquinone $FAD^{\bullet-}$ to the neutral semiquinone $FADH^{\bullet}$ [9,10]. On the other hand, the neutral semiquinone $FADH^{\bullet}$ state is meta-stable at room temperature under aerobic conditions[22]. Accordingly, static, or steady-state, datasets for the substrates and products of both electron transfer reactions, i.e. oxidized, neutral semiquinone, and fully reduced states, could be produced via controlled exposure to light and/or reducing agents followed by data collection without illumination. Notably the unstable anionic semiquinone state was an exception, as it could only be obtained via TR-SFX. Meanwhile, the TR-SFX experiments of the two photoreduction steps could be performed separately, leading to 23 structures (Str1-Str23 in Tables 1 and S1-S3, and Figs. S1 and S2). Each structure is designated as $E_{X/Y}$, with subscript X referring to the initial redox status (ox for oxidized, FAD_{ox}; semi for semiquinone, $FADH^{\bullet}$; and red for reduced, $FADH^{-}$), and subscript Y describing their data collection mode ("ss" for steady state, "dark" for a non-illuminated TR control structure, and time for the delay after illumination). Furthermore, difference electron density maps[37] were constructed to highlight structural differences, which are designated as the difference between two states, $E_{X'/Y'}$-$E_{X/Y}$.

To monitor structural changes of the FAD isoalloxazine moiety, we introduce the ρ_C and ρ_N dihedral angles (Fig. 1d). These changes happening upon FAD reduction were so far called butterfly bending and defined as the angle (α) between the normal vectors of the A and C ring planes (Fig. 1d)[38]. Values close to zero degrees were derived for the oxidized flavin state, and values of 15°-25° for the reduced hydroquinoid state of several flavoproteins[39–41]. However, α

cannot discriminate between longitudinal twisting (bending along the long axis crossing the A, B and C rings) and lateral bending or butterfly-like "buckling" (bending along the short *N5-N10* axis)[38], whereas ρ_C and ρ_N can. When buckling dominates, $\rho_C \approx \rho_N \approx \alpha$; conversely, $\rho_C \neq \rho_N$ indicates a twist of the isoalloxazine moiety.

Table 1. Primary properties of the *Mm*CPDII TR-SFX structures.

Str. no.	Str. name	redox state	ρ_C angle	ρ_N angle	distance FAD*N5*-R378*Nε* (Å)[b]	distance FAD*N5*-N403*Oδ* (Å)[c]	PDB code	resolu-tion (Å)[d]
0[a]	$E_{ox/sync}$	FAD_{ox}	7.6°	8.7°			7F8T[e]	1.50
1	$E_{ox/ss}$	FAD_{ox}	2.0°	2.0°	4.8	3.3	6LT3	2.25
First time-resolved series (FAD_{ox} → $FAD^{\bullet-}$)								
2	$E_{ox/dark}$	FAD_{ox}	2.0°	2.0°	4.8	3.4	6LM4	2.0
3	$E_{ox/10ns}$	$FAD^{\bullet-}$	-3.6°	0.8°	4.7	3.6	6LMB	2.55
4	$E_{ox/50ns}$	$FAD^{\bullet-}$	3.7°	6.6°	4.6	3.6	6LM5	2.25
5	$E_{ox/250ns}$	$FAD^{\bullet-}$	17.1°	11.1°	4.6	3.7	6LM6	2.4
6	$E_{ox/1\mu s}$	$FAD^{\bullet-}$	9.5°	13.4°	3.4	4.0	6LM7	2.2
7	$E_{ox/10\mu s}$	$FAD^{\bullet-}$	30.9°	14.4°	3.2	3.7	6LM8	2.25
8	$E_{ox/125\mu s}$	$FAD^{\bullet-}$	20.3°	18.8°	3.4	4.2	6LMC	3.0
9	$E_{ox/400\mu s}$	FAD_{ox} /$FAD^{\bullet-}$	5.6°	4.8°	4.5	3.4	6LM9	2.4
10	$E_{ox/1ms}$	FAD_{ox}	4.4°	3.1°	4.5	3.4	6LME	3.0
11	$E_{ox/5ms}$	FAD_{ox}	3.3°	4.5°	4.8	3.4	6LMA	1.9
Protonation step ($FAD^{\bullet-}$ → $FADH^{\bullet}$)								
12	$E_{semi/ss}$	$FADH^{\bullet}$	4.6°	4.75°	3.9	2.7	6LT1	2.1
Second time-resolved series ($FADH^{\bullet}$ → $FADH^{-}$)								
13	$E_{semi/dark}$	$FADH^{\bullet}$	5.3°	4.7°	3.9	2.7	7CLW	2.10
14	$E_{semi/10ns}$	$FADH^{-}$	9.7°	8.8°	4	2.5	7C3P	2.15
15	$E_{semi/30ns}$	$FADH^{-}$	11.3°	11.5°	3.6	2.7	7C3R	2.1
16	$E_{semi/100ns}$	$FADH^{-}$	11.3°	9.6°	3.7	2.8	7C3W	2.3
17	$E_{semi/300ns}$	$FADH^{-}$	16.5°	16.8°	3.4	2.7	7C3X	2.5
18	$E_{semi/1\mu s}$	$FADH^{-}$	9.7°	9.7°	3.6	2.6	7CLM	2.1
19	$E_{semi/5\mu s}$	$FADH^{-}$	12.7°	11.5°	3.7	2.8	7CLN	2.1
20	$E_{semi/10\mu s}$	$FADH^{-}$	8.5°	8.5°	3.9	2.6	7CLO	2.1
21	$E_{semi/30\mu s}$	$FADH^{\bullet}$ /$FADH^{-}$	10.9°	10.6°	3.8	2.7	7CLP	2.1
22	$E_{semi/100\mu s}$	$FADH^{\bullet}$	5.3°	5.5°	3.9	2.6	7CLQ	2.15
Full reduction at steady state								
23	$E_{red/ss}$	$FADH^{-}$	14.3°	14.5°	3.3	3.1	6LT2	2.20

[a]Previously reported structure from synchrotron X-ray data[23]. The dihedral angles were not reported, and were obtained from refining by our procedures.

[b]The FAD*N5*-R378*Nε* distance is between the FAD isoalloxazine *N5* atom and the Arg378 *Nε* atom.

[c]The FAD*N5*-N403*Oδ* distance is between the FAD isoalloxazine *N5* atom and the Asn403 *Oδ1* atom.

[d]Resolution values given here correspond to the extrapolated structure factor dataset.

[e]This structure is derived from 2XRY with dihedral angles refined by the approach of this work.

The damage-free structure of oxidized *Mm*CPDII

Like the structure of $E_{ox/sync}$, previously solved by conventional synchrotron X-ray crystallography[10] (Str0 in Table 1), our steady-state oxidized structure $E_{ox/ss}$ (Str1), solved at room temperature by SFX, consists of a two-domain topology (Fig. 2a), with the isoalloxazine-interacting elements being the hydrophobic side of helix α16 and sidechains of Asn403, Arg378, and Asp409 (Fig. 2b). However, the isoalloxazine ring of our $E_{ox/ss}$ is only slightly buckled with ρ_C, ρ_N dihedrals of 2.0° and 2.1° (Fig. 2c), substantially smaller than that of 7.6° and 8.7° for the synchrotron structure $E_{ox/sync}$ as processed by our approach for comparison with TR-SFX structures (Fig. 2d). The difference can be attributed to $E_{ox/ss}$ being the purely oxidized form as characterized by *in crystallo* UV-Vis absorption spectra (Fig. S3a), whereas $E_{ox/sync}$ has been partially reduced by synchrotron X-ray irradiation as supported by *in crystallo* spectra[23]. In addition, as shown in Table 1, the $E_{ox/dark}$ structure (Str2, time zero) is nearly identical to the steady-state $E_{ox/ss}$ structure, providing validation for the TR-SFX experiments.

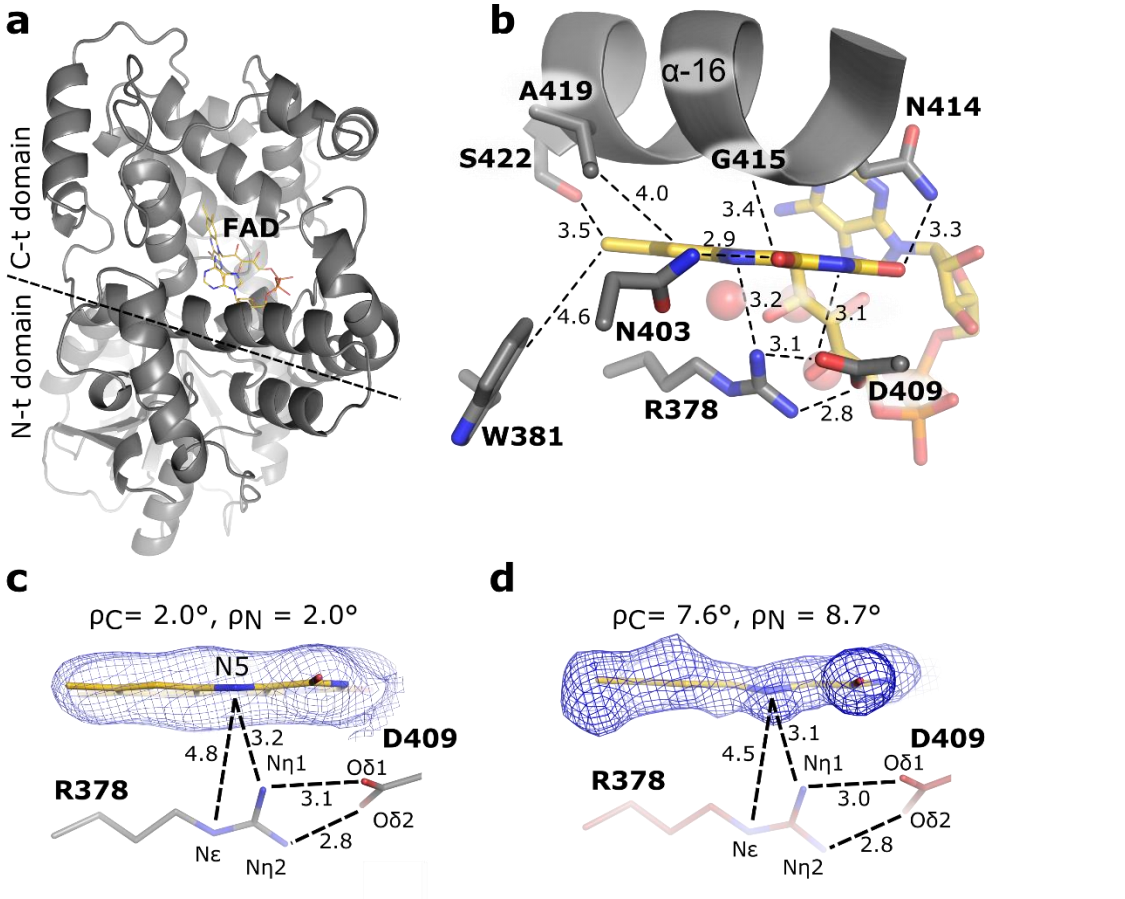

152

Figure 2. Structure of oxidized *Mm*CPDII photolyase. (**a**) Global structure of $E_{ox/ss}$ (Str1, steady state oxidized) showing the overall fold with FAD depicted in gold. (**b**) Isoalloxazine binding pocket with interacting residues (grey sticks) and waters (red spheres). None of the waters are within the hydrogen bonding distance to N5. (**c**) Geometry of the $E_{ox/ss}$ FAD isoalloxazine ring showing minor buckling. (**d**) Geometry of the isoalloxazine ring from the synchrotron X-ray structure $E_{ox/sync}$ (Str0)[23] after reprocessing with our approach, showing increased buckling angles due to radiation-induced photoreduction. In c-d, SigmaA-weighted 2mF_{obs}-DF_{calc} omit maps surrounding the isoalloxazine moiety (blue mesh, 1σ contour level) are shown.

153

154 **Changes in active site structures following ET**

155 In both photoreduction steps, structural changes of the isoalloxazine ring and its surrounding
156 residues occur after ET, from the first time-point at 10 ns up to roughly 1-10 μs. Detailed
157 analyses indicate that these structural changes involve mainly the geometry of the isoalloxazine
158 ring, the Arg378-Asp409 salt bridge underneath it, and the sidechain of Asn403 close to the

isoalloxazine N5 atom, which are summarized in Table 1. The time courses of the changes in structural parameters from Table 1 are plotted in Figure 3a,c (RS1) and b,d (RS2), while representative structures and difference density maps are shown in Figure 3e,h (RS1), g,j (RS2), and f,i (the protonation step, PS), which will be addressed in subsequent sections.

On the other hand, the ETC tryptophans (Fig. 1b) are not a subject of this study as there are no significant structural changes in either of our time-resolved series (Fig. S4a,b), in agreement with previous spectroscopic studies indicating that, for *Mm*CPDII, the initial light-driven electron transfer completes in less than a nanosecond[10]. Interestingly, we did observe conformational changes of a few residues (H343, H356, and N361) surrounding Trp388 around the first time-point of 10 ns (Fig. S4c,d), supporting that electron transfer and structural changes in a redox reaction can be dissected by TR-SFX.

Changes in the isoalloxazine geometry

During RS1, the FAD_{ox} to $FAD^{\bullet-}$ transition (Fig. 3a), ρ_C values change from 10 ns, reaching a maximum at 10 μs, whereas ρ_N values follow the same pattern but with milder changes, suggesting a twist. On the other hand, from 125 μs after photoexcitation, ρ_C and ρ_N have both decreased substantially, and by 400 μs have returned to their initial values, correlating well with the reversion of structural changes in the vicinity Trp388 (Fig. S4c,d). This apparently reflects $FAD^{\bullet-}$ reoxidation via back electron transfer toward $Trp388^{\bullet}$ (Fig. 1a, b), as under our experimental conditions the transiently formed tryptophan radical is present due to the lack of external reductants[9,10]. As indicated by kinetic data[10], the estimated half-life of $FAD^{\bullet-}$ is less than a millisecond (Fig. S3b).

During RS2 ($FADH^{\bullet}$ to $FADH^{-}$, Fig. 3b), the ρ_C and ρ_N dihedral angles increase together with time and reach a maximum at 300 ns (16.5° and 16.8°, respectively, Table 1), correlating fairly well with the values in the fully reduced steady-state $E_{red/ss}$ (14.3°, 14.5°, respectively).

However, they are both reverted to ~7° by 100 µs, again indicating the onset of reoxidation of the isoalloxazine ring. Accordingly, difference maps relative to $E_{red/ss}$ (Fig. 3g and Fig. S2a) show a negative density peak below the central ring B of the isoalloxazine, which decreases to the noise level (3σ) past 300 ns and increases again past 10 µs (Fig. 3d, magenta curve). Importantly, observation of the parameters reaching a peak and relaxing back in Figure 3a-d provides further support that the observed small changes are significant and mirror reversible redox-dependent changes. In summary, the time-resolved structural analysis of both photoreduction steps illustrates how, after initial ET, the isoalloxazine moiety re-hybridizes to its new redox state and reaches its final structure in about one to ten microseconds. Our results above expand the description of a redox reaction of FAD to include subsequent structural changes in addition to the ET steps.

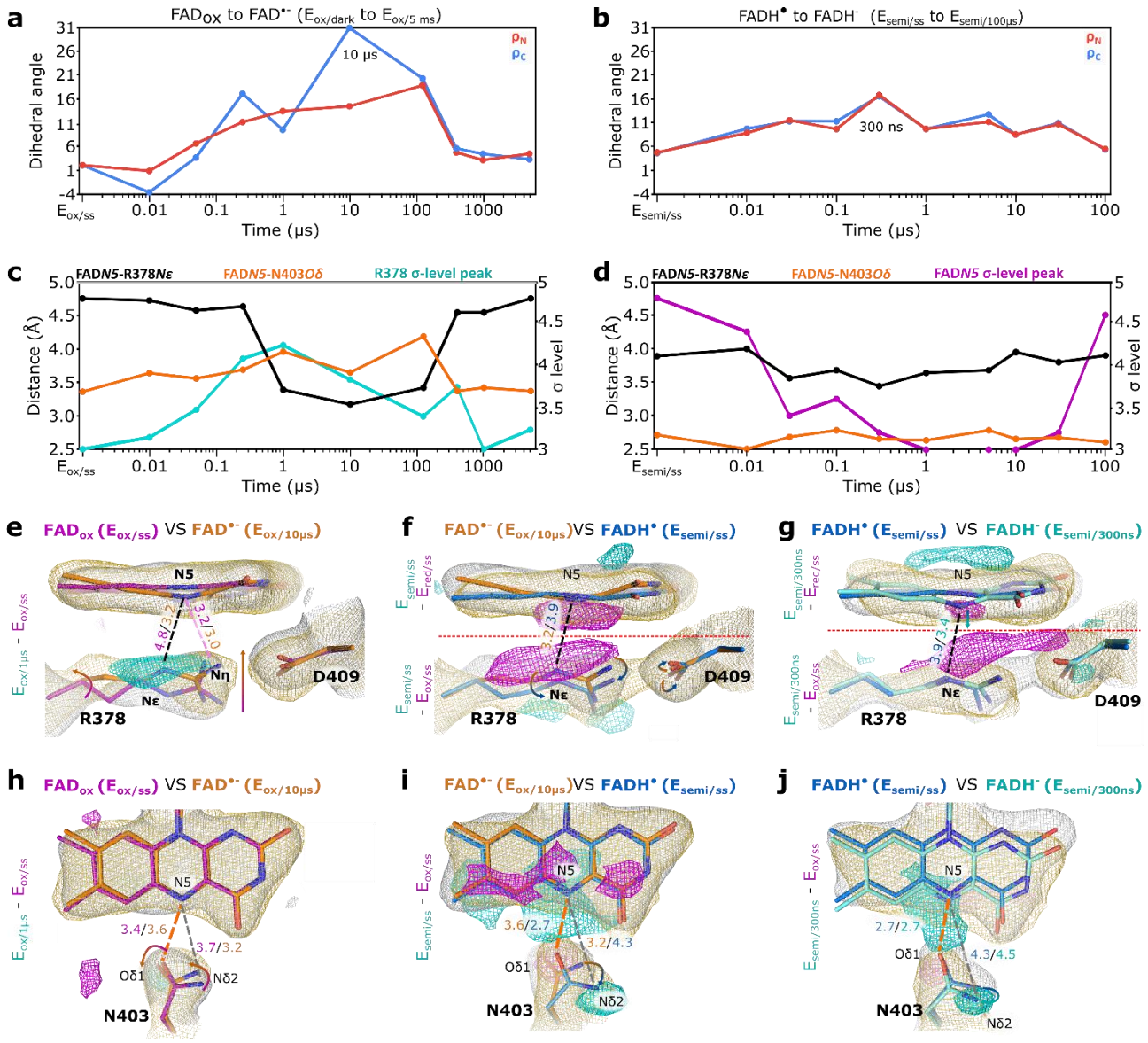

Figure 3. **Structural changes during the photoactivation of *Mm*CPDII.** (**a,b**) Evolution of ρ_C (blue) and ρ_N (red) dihedral angles over time for photoreductions 1 and 2, respectively. (**c,d**) Evolution over time of the FAD*N5*-R378*Nε* (black curve) and FAD*N5*-N403*Oδ* distances (orange curve), along with plots of the σ-levels of the positive difference peak near R378*Nε* (c, cyan curve) and the negative difference peak below FAD*N5* (d, magenta curve). (**e-g**) Structures of the isoalloxazine ring and the nearby Arg378-Asp409 salt bridge at the beginning and end of each photoreduction step. For RS1 (e), $E_{ox/ss}$ (FAD_{ox}) is superposed with $E_{ox/10\mu s}$ ($FAD^{\bullet-}$), for PS (f), $E_{ox/10\mu s}$ ($FAD^{\bullet-}$) with $E_{semi/ss}$ ($FADH^{\bullet}$), and for RS2 (g), $E_{semi/ss}$ ($FADH^{\bullet}$) with $E_{semi/300ns}$ ($FADH^{-}$). Each panel is also superposed with 2σ contoured 2DFo-mFc omit maps corresponding to the beginning (grey) and end (gold) states of each photoreduction step, as well as difference maps as indicated by the vertical labels left to the structural moiety. Difference map contour levels: (e) 3σ, (f-g) 3.5σ near the isoalloxazine moiety (above the red dotted line) and 4.0σ near the salt bridge (below the red dotted line). (**h-j**) Redox- and time-dependent FAD N5-Asn403 interaction for the same structures as in e-g, respectively. Omit maps as above, as well

as difference maps relative to $E_{ox/ss}$ (4σ) are also shown. In all structures, arrows indicate motion, while dotted lines the FAD*N5*-R378*Nε* (black) and FAD*N5*-N403*Oδ* (orange) distances in Å. In all difference density maps, cyan indicates positive and magenta indicates negative.

Conformational changes of Arg378 concurrent with bending of FAD isoalloxazine ring

For RS1, a positive peak (from difference maps relative to $E_{ox/ss}$) appears above Arg378 *Nε* (Fig. 3e and Fig. S1a). When its σ-level is plotted against time (cyan curve in Fig. 3c), it reveals a progressive change peaking at 250 ns to 10 μs, followed by a back relaxation till 1-5 ms, suggesting a movement of Arg378 *Nε* toward the *N5* atom of FAD concurrent with bending and subsequent relaxation of the isoalloxazine ring. In agreement, the FAD*N5*-R378*Nε* distance (Table 1) decreases and then reverts back following the same pattern (Fig. 3c, black curve). Importantly, structural analyses indicate that while Arg378 *Nε* moves toward FAD *N5*, the bifurcated Arg378-Asp409 salt bridge remains in place (Fig. 3e and Fig. S1a).

The same correlation between the FAD*N5*-R378*Nε* distance and isoalloxazine bending was also observed in RS 2 ($FADH^{\bullet}$ to $FADH^{-}$). As shown by the black curve in Figure 3d, the distance becomes progressively shorter, reaching a minimum at 300 ns where isoalloxazine bending is most pronounced (Fig. 3b), and again relaxes back to the starting point at 100 μs. However, the change in the FAD*N5*-R378*Nε* distance in the second set is smaller than that in the first set (black curves in Fig. 3c,d). Accordingly, the closing between FAD *N5* and R378 *Nε* in the second set is likely caused mainly by the out-of-plane movement of FAD *N5*. In support, the Arg378 sidechain remained unmoved during RS2 as explained below. Meanwhile, the structural changes and the two different mechanisms described above for the two TR-SFX series and additional results below can be visualized in Videos S1 and S2.

Protonation of $FAD^{\bullet-}$ and weakening of the Arg378-Asp409 salt bridge

Protonation of $FAD^{\bullet-}$ at the *N5* position is essential for the photoactivation, as only the neutral semiquinone $FADH^{\bullet}$ can be further reduced to the active $FADH^{-}$ state (Fig. 1a). However, the proton donor and molecular mechanism remain elusive[42]. Our structural data points toward a close involvement of the Arg378-Asp409 salt bridge in this step, as its geometry is strongly affected by the $FAD^{\bullet-}$ protonation. As shown in Figure 3f, the Arg378 guanidinium moiety moves away from the isoalloxazine ring after the $FAD^{\bullet-}$ to $FADH^{\bullet}$ conversion, reverting to a similar position to the oxidized state. However, the geometry of the bifurcated salt bridge is altered by this $FAD^{\bullet-}$ to $FADH^{\bullet}$ conversion, causing Arg378 sidechain to break its salt bridge with Asp409 with a swivelling motion (Fig. 3f). In support, difference maps from the second series, relative to $E_{ox/ss}$, reveal a very clear negative signal above the Arg378 sidechain (Fig. 3g and Fig. S2b), in contrast to the positive difference peaks in the first photoreduction step (Fig. 3e and Fig. S1a). Meanwhile, no significant peaks were observed relative to the fully reduced state $E_{red/ss}$ (Fig. S2a). Furthermore, the intensity of the above mentioned negative difference map peak remained approximately constant (Fig. S2b), and additional difference map peaks surrounding guanidinium-carboxylate appeared (Fig. 3f-g).

These results, along with absence of other efficient proton donors or water molecules within hydrogen bonding distance to the isoalloxazine *N5* nitrogen (Fig. 2b), suggest that Arg378 is likely the proton donor for the protonation of $FAD^{\bullet-}$ to $FADH^{\bullet}$. In support, the Arg378-Asp409 ionic pair is highly conserved, as database analysis of all known photolyase-cryptochrome family (PCF) sequences (19524) showed that only three class II photolyases and six cryptochromes lack this Arg-Asp salt-bridge. Our attempt to construct these unusual natural mutants resulted in either protein aggregation or loss of FAD binding (Tables S4-S5). Only the conservative R378K mutation yielded a well-behaved, monodisperse protein capable of FAD uptake, but at only ~20% stoichiometry (Fig. S5a) and with non-specific binding (Fig. S5b).

These results explain why a key function for this highly conserved pair [43–45] has never been reported before for any member of the PCF.

Facilitation of protonation and stabilization of the protonated state by Asn403

The *N5* nitrogen of free $FADH^{\bullet}$ has been shown to be a weak acid (pK_a 8.5)[42], which is insufficient for its conjugate base $FAD^{\bullet-}$ to drive proton transfer from Arg378 (pK_a ~12.5). However, a previous report showed that the pK_a of the *N5* nitrogen of flavodoxin's semiquinone $FMNH^{\bullet}$ coenzyme is raised to >13 due to an H-bond with a backbone carbonyl oxygen[45]. A similar interaction between isoalloxazine *N5* of $FADH^{\bullet}$ and the equivalent of *Mm*CPDII Asn403 *Oδ1* atom has been reported by FT-IR studies of other photolyases[43,44], a behavior we can now explain with our structures: In FAD_{ox}, Asn403 *Oδ1* is closer to FAD_{ox} N5, while *Nδ2* mainly interacts with the carbonylic FAD_{ox} *C4=O*. During RS1, photoreduction to $FAD^{\bullet-}$ causes the Asn403 amide sidechain to rotate, with *Oδ1* moving away from N5, while *Nδ2* approaching it (Fig. 3h). Upon protonation to $FADH^{\bullet}$ (Fig. 3i), the Asn403 sidechain swivels, bringing the Asn403 *Oδ1* atom in close proximity to the N5-H, whereas *Nδ2* moves to a distal position, which nevertheless allows it to continue interacting with *C4=O* (Fig. S2c). In accordance with FT-IR data, the $FADH^{-}$ state structure (Fig. 3j) is somewhat in-between, as the Asn403 swivel is partially maintained. Although previous mutagenesis studies of Asn403 in *Mm*CPDII suggested an important role in photoreduction[23], our results provide structural evidence for stabilization of the protonated state by H-bonding between isoalloxazine *N5* and Asn403 *Oδ1*, and support an unusually high pK_a for the $FADH^{\bullet}$ *N5* position in photolyase.

Furthermore, the comparison between the FAD isoalloxazine *N5* to Asn403 *Oδ1* distance (FAD*N5*-N403*Oδ* distance, orange curves in Fig. 3c-d) and the FAD*N5*-R378*Nε* distance (black curves in Fig. 3c-d) shows an inverse relationship in both TR sets. Together, the results suggest that, during RS1, Arg378 approaches the $FAD^{\bullet-}$ isoalloxazine *N5* but Asn403 *Oδ1*

recedes away. During PS, Arg378 moves away whereas Asn403 *Oδ1* moves in to form an H-bond with the isoalloxazine *N5*-H. Then, upon RS2, isoalloxazine *N5* moves again toward Arg378 due to enhanced buckling, leading to slight lengthening of the H-bond with Asn403 *Oδ1*. As shown in Table 1 and Figure S2b, the $E_{semi/300ns}$ structure is strikingly similar to the steady-state reduced structure $E_{red/ss}$. These results indicate intricate coordination between Arg378 and Asn403 to mediate the two photoreduction and protonation steps and stabilize the intermediate species in the process.

The FAD redox sensor triad and the overall mechanism of photoactivation

Our data shows how Asn403, Arg378 and Asp409 function closely as an "FAD redox sensor triad" to mediate structural changes of the FAD isoalloxazine, from ns to μs after the initial electron transfer in both photoreduction steps and the in-between protonation step. The structural changes are small (Fig. 4a), but they have been exquisitely dissected by a large number of TR-SFX structures with continuous changes and intricate coordination involving an extensive H-bonding network (Fig. 4b). While Figure 3a-d show complete forward reaction and back relaxation for each photoreduction step separately, here we merge the two forward reactions and address the overall mechanism in four ways: H-bond analysis to show the variation of each H-bond in each intermediate structure (Fig. 4c), structural schematics based on the results of individual steps (Fig. 4d), merging of dihedral angles and interatomic distances from Figure 3 (Fig. 4e), and visual illustration (Video S3). These analyses together are explained below.

In RS1, i.e. the transition from FAD_{ox} to $FAD^{\bullet-}$, a negative charge builds up at FAD *N5*, electrostatically repulsing the Asn403 *Oδ1* atom and attracting both Asn403 *Nδ2* and, more importantly, the positive Arg378 sidechain in preparation for protonation. The result is a transient H-bond between the proximal Arg378 *Nη* and FAD *N5* (Figs. 3e, 4c-d). Accordingly,

between 1 μs and 125 μs ($FAD^{\bullet-}$), the FAD*N5*-R378*Nε* distance is the shortest (i.e. the most stabilized isoalloxazine moiety), whereas the FAD*N5*-N403*Oδ* distance is the longest (i.e. the least degree of destabilization) (Figs. 3c, 4e).

When the sidechain of Arg378 is close enough to FAD *N5*, proton transfer occurs. $FADH^{\bullet}$ and Arg378, now both neutral, interact only weakly with each other, with Arg378 receding from the isoalloxazine moiety and the Asp409 sidechain (Fig. 3f). Instead of behaving as an ionic pair, the Arg378 and Asp409 are now connected by a single H-bond (Fig. 4c-d). A driving force for the FAD *N5* protonation is its interaction with Asn403 *Oδ1*, which moves in to form an H-bond, becoming the main stabilizing element for the neutral semiquinone state (Fig. 3i, $E_{semi/ss}$, FAD*N5*-N403*Oδ* distance 2.7 Å).

Then, in RS2, the same trends are observed, with Asn403 *Oδ1* moving slightly away but still maintaining the hydrogen bond, while isoalloxazine buckling closes the gap to Arg378 *Nε*, reaching maximal changes at 300 ns to 1 μs (Figs. 3d, 3g, 4c-e) and resulting in a very close approximation of the steady-state $E_{red/ss}$, which represents the fully reduced $FADH^-$ state, and where both FAD*N5*-N403*Oδ* and FAD*N5*-R378*Nε* H-bonds contribute to the stabilization of $FADH^-$.

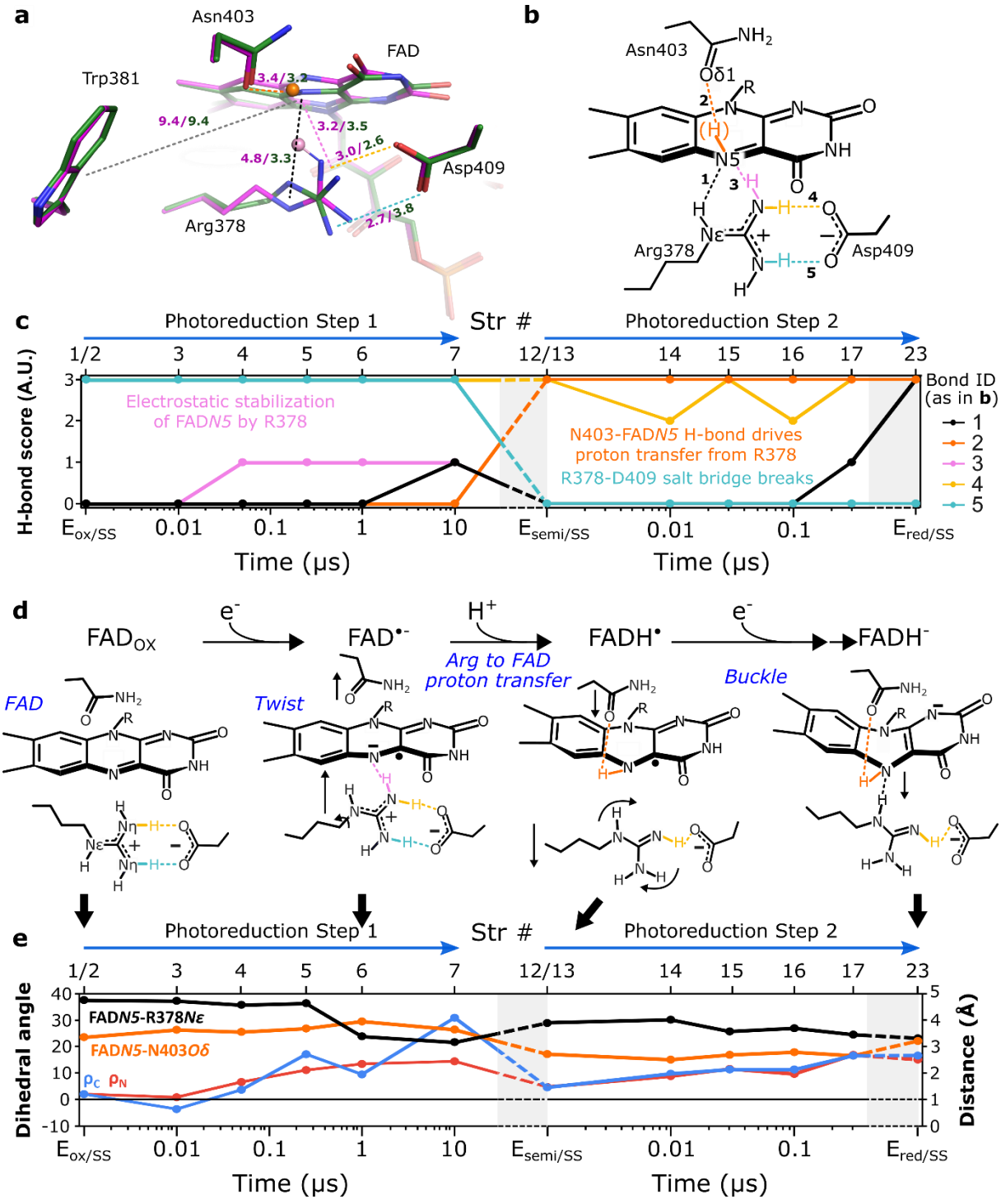

Figure 4. Mechanistic view of *Mm*CPDII photoactivation. (**a**) Superposed active site structures of *Mm*CPDII in the oxidized (purple) and reduced (green) states. The pink ball-and-stick model designates the proposed Arg378 proton to be transferred to FAD *N5*, the orange after transfer. Distances of interest are color coded as dashed lines, with the black one corresponding to the FAD*N5*-R378*Nε* distance, while the orange one the FAD*N5*-N403*Oδ* distance. (**b**) Schematic representation of key elements in the Asn403-isoalloxazine-Arg378-Asp409 H-bonding network. Bonds of interest are labeled by a number and a color. (**c**) Plots summarizing the dynamic behavior of the H-bonding network. Line colors

on the graph follow those in (b). H-bond scores are based on a previous PDB-wide analysis and described in Methods. Briefly, a score of 1 indicates three necessary conditions have been met, while 2, 3 indicate additional favorable conditions. The top axis indicates structure numbers from Table 1. (**d**) Structural schematics of the redox and protonation reactions. Only the relevant hydrogen bonds for each state are shown, color coded as in b and c. (**e**) Merging of the dihedral angles and distance plots from Figure 3a-d, showing continuous changes in the entire photoactivation process (i.e., by excluding the back relaxation time points). In both c and e, a grey background indicates reaction steps whose timing is not well defined by our experiments.

Discussion

Overall, this work describes the first structural description of the microscopic processes of the photoreduction of a DNA photolyase, highlighting geometric changes of the isoalloxazine moiety in the re-hybridization process, how they are mediated by Asn403/Arg378-Asp409, which we name a redox sensor triad, and enable a typical quinone chemistry, namely sequential pumping of two electrons separated by a protonation step. The X-ray damage-free structure of *Mm*CPDII shows that the catalytically active $FADH^-$ chromophore adopts a bending angle of about 14°, and that bending of the $FADH^-$ isoalloxazine delicately controls the ET potential by affecting forward as well as backward electron transfers. Although the observed bending in the photolyase is well below the degree of bending of $FADH^-$ in free solution (24°-33°)[46], it is significant for the DNA repair mechanism of photolyases as most previous theoretical calculations on ET reactions between the isoalloxazine and the CPD and (6-4) DNA lesions predicted planarity of the isoalloxazine due to a lack of interaction with the protein matrix in QM models[47]. Planarity was also postulated from the photochemistry of catalytically competent photolyases in the $FADH^-$ state[8], because flexible butterfly motions across conical sections would cause rapid deactivation of excited $FADH^{-*}$ states rather than electron transfer to the bound DNA lesion. Our structures of the $FADH^-$ state show that these flexible motions can be avoided by increased interaction with the arginine and asparagine of the redox triad,

thus leading to a higher rigidity of the flavin binding site and explaining the bathochromically shifted and lifetime-elongated fluorescence emission spectra of $FADH^-$ in photolyases when compared to free solution[8].

In terms of the photoreduction to $FADH^-$, four features of its molecular mechanism are fundamental for not only photolyases, but also other flavoenzymes. First, electron uptake in small molecules in solution and in photolyases by FAD takes place at similar time-scales[9,48] with subsequent geometric changes requiring only picoseconds in the former[48]. However, we found that the equivalent response of the protein-embedded isoalloxazine moiety is delayed by nanoseconds to microseconds. This can now be explained by the role of the protein matrix for stabilizing otherwise highly unstable intermediates such as $FAD^{\bullet-}$ by allowing them to probe a wide region of the conformational space via twisting and buckling. These transient structural changes increase the probability of ulterior reactions, first triggering of proton transfer (PT) to form $FADH^{\bullet}$ and then further photoreduction to $FADH^-$. This conclusion extends previous theoretical studies, which proposed that buckling and twisting motions in the isoalloxazine ring just serve for controlling the redox chemistry of flavins[38]. We found that they can also actively participate in PT pathways with the embedding protein matrix, thus highlighting the role of the protein in controlling quinone chemistry.

Secondly, our data uncovered a redox sensor triad Asn/Arg-Asp. A structure-based PDB wide survey in which we searched for flavoproteins presenting an Arg-Asp(Glu) pair nearby their isoalloxazine moieties returned only PCF members, supporting the unique functional roles of this conserved motif. Interestingly, within PCF, the third residue, asparagine, is conserved in enzymatically active photolyases, but not in solely photosensory cryptochromes, where this residue can be replaced by aspartate like in plant cryptochromes or cysteine in insect cryptochromes[49]. In those with alternative redox triads (Asp/Arg-Asp and Cys/Arg-Asp), the quinone chemistry is significantly affected, with photoreduction leading to single electron

uptake and protonation to $FADH^{\bullet}$ in the former[50], while the latter arrests photoreduction in the $FAD^{\bullet-}$ [51].

Thirdly, despite its high sidechain pKa, the function of arginine as a proton donor has been suggested for several enzymes [52–56]. Our results provide structural intermediates before and after protonation of isoalloxazine *N5* by Arg378 in the *Mm*CPDII photolyase. Furthermore, widening the above-mentioned PDB search for non-protein acidic ligands nearby an arginine and a flavin revealed six flavin-dependent oxidoreductase families (Table S6) with specific examples from each family shown in Figure S6, including the fumarate reductase mentioned above[52] and suggesting a potentially wide catalytic role for such an arrangement.

Finally, intramolecular ET reactions in photolyases were often understood as simplest biological model systems for comparable processes during the light-driven charge separation in photosynthetic reaction centres. The uptake of electrons and protons by quinone substrates in the Q_B binding site is known to follow an ordered ET-PT-ET-PT scheme[5], thus being comparable to the ET-PT-ET scheme of photolyases, and is accompanied by a redox-dependent move of Q_B from a distal to a proximal binding site. Notably, protonation of $Q_B^{\bullet-}$ as formed after first ET is supposed to occur via a serine, Ser-L223 in bacterial reaction centres[57]. Given our unexpected finding that an arginine conserved in the PCF serves as proton donor to the flavin cofactor, but not the other candidate asparagine of the redox triad, we expect that similar time-resolved structural studies will be necessary in future to nail down PT events in other complex biological redox systems, e.g. the photosynthetic reaction centres.

Methods

Protein production, crystallization and preparation for XFEL

Protein was produced, and crystals were obtained, by upscaling previously published conditions[23]. Concentrated crystal slurries were produced by centrifugation of crystallization batches. For obtaining a fully oxidized dataset, the crystal slurry was then embedded in a hydrophobic grease matrix in a 1:9 crystal:matrix ratio, as described elsewhere[58]. After this point, the sample was maintained under far red light (650 nm) at all times to avoid in-situ photoreduction.

For obtaining the semiquinone crystalline material used to acquire the $E_{semi/ss}$, $E_{semi/dark}$ and all $E_{semi/t}$ structures (Table 1), the crystal slurry was first supplemented with 50 mM DTT. For full reduction, the crystal slurry was then exposed to bright white light (Leica KD300) for 5 minutes, and then for partial oxidation to air for another 20 minutes, followed by embedding in grease matrix. The production and handling of fully photoactivated *Mm*CPDII crystals ($E_{red/ss}$) was analogous to semiquinone, but to avoid oxidation, the entire procedure was performed under anaerobic conditions.

Data collection.

All 23 structures (Str1-Str23 in Tables 1 and S1-S3 and Figs. S1 and S2) were obtained at the SPring-8 Angstrom Compact free electron LAser (SACLA)[59], with crystals being excited via a nanosecond pulse from a 408 nm OPO laser running at 15 Hz, while data collection from XFEL pulses at 30Hz.

Data processing and structural solution

All collected images were initially sorted on-site with cheetah[60], and then processed off-site with CrystFEL 0.6.2[61]. Processed datasets were then scaled via SCALEIT, a piece of software within the CCP4i crystallographic suite[62]. Molecular replacement structural solution was performed for $E_{ox/ss}$ via Phaser, also part of CCP4i, using the original $E_{ox/sync}$[23] (PDB code 2XRY) as the search model. Further datasets were then solved based on $E_{ox/ss}$, or its derived structures.

Overall refinement and structural data visualization

Structure factor extrapolation[31,36,63] was used to refine the subtle time- and redox-dependent structural changes (Fig. S1 and S2 for the two time-resolved series). Furthermore, difference

electron density maps[37] were constructed to highlight these structural differences, which are designated as the difference between two states, $E_{X'/Y'}$-$E_{X/Y}$. Quantitative analysis of difference map peaks was normalized to σ levels, i.e. the factor by which a peak's magnitude exceeds the background electron density. Our results showed that significant difference maps were only observed in the active site region as shown by examples in Figures S7 and S8. Meanwhile for RS1, ultrafast conformational changes around 10 ns also occurred in the vicinity of Trp388, the final electron donor in the electron transfer chain, in the absence of an external reducing agent (Fig. S4c,d). Since RS2 was performed in the presence of reducing agent DTT, W388• can be regenerated to W388 and the ultrafast conformational change could not be observed.

Refinement of the FAD isoalloxazine moiety and its conformational changes

To follow the bending of FAD in our structures, and avoid model bias, the dihedral angles for all structures, as listed in Table 1, were calculated by adapting previous real space correlation methods established for the analysis of TR-SFX data as it applies to subtle changes in photoreceptor chromophores[36,64,65]. Briefly, an equilibrium ensemble for the FAD redox dependent conformational space was computationally generated based on the $E_{ox/ss}$, $E_{semi/ss}$ and $E_{red/ss}$ datasets, from which minimum and maximum ρ_C and ρ_N values (Fig. 1d) could be determined. Then, ρ_C and ρ_N restraints within those limits were applied stepwise to each dataset via three cycles of Phenix refinement[66] using the corresponding resting structure as the initial model (Fig. S9). The software sfall was then employed to produce calculated structure factors from both the initial (Fci) and refined (Fcref) models, and Fcref-Fci maps within 2.5 Å of the isoalloxazine moiety were calculated using the initial model phases, analogously to the experimental maps presented in e.g. Figure 3. Finally, in order to assess the quality of the resulting isoalloxazine geometry, the real space correlation coefficient (CC) between the Fcref-Fci and the corresponding $F_{X'/Y'}$-$F_{X/Y}$ maps was calculated. Accordingly, we could produce heat maps where ρ_C and ρ_N values were correlated to the CC, to the degree they were able to reproduce the observed difference density features. A final set of restraints for each individual structure was then generated as the average and standard deviation of the ρ_C and ρ_N with the top CC score, and all those with at least 95% of that score (Fig. S9). A detailed description of these and other analysis procedures can be found in Supplementary Methods.

***In crystallo* UV/Vis absorption spectroscopy**

In crystallo UV/Vis absorption spectroscopy was performed at the ID29S-Cryobench Laboratory, ESRF, Grenoble, France[67]. Here, crystals were treated as for the steady-state XFEL experiments (see above) to photoreduce them into the different redox states. Samples were then directly mounted on the Cryobench goniometer at 100 K under constant nitrogen gas flow. All data was acquired with a 25 µm focal point for the probing white light beam, while the detector optics was connected to the outgoing objective via a 200 µm-diameter optical fiber. Individual acquisition times were 200 ms, with ten acquisitions being averaged per spectrum.

References

1. Belevich, I., Bloch, D. A., Belevich, N., Wikström, M. & Verkhovsky, M. I. Exploring the proton pump mechanism of cytochrome c oxidase in real time. *Proceedings of the National Academy of Sciences of the United States of America* **104**, 2685–2690 (2007).
2. Field, C. B., Behrenfeld, M. J., Randerson, J. T. & Falkowski, P. Primary production of the biosphere: Integrating terrestrial and oceanic components. *Science* **281**, 237–240 (1998).
3. Sun, F. *et al.* Crystal structure of mitochondrial respiratory membrane protein Complex II. *Cell* **121**, 1043–1057 (2005).
4. Alberts, B. *et al.* Electron-Transport Chains and Their Proton Pumps. (2002).
5. Nicholls, D. G. & Ferguson, S. J. Respiratory Chains. in *Bioenergetics* 91–157 (Elsevier, 2013). doi:10.1016/b978-0-12-388425-1.00005-1.
6. Entsch, B. & Ballou, D. P. Flavins. in *Encyclopedia of Biological Chemistry: Second Edition* 309–313 (Elsevier Inc., 2013). doi:10.1016/B978-0-12-378630-2.00014-1.
7. Wang, J., Du, X., Pan, W., Wang, X. & Wu, W. Photoactivation of the cryptochrome/photolyase superfamily. *Journal of Photochemistry and Photobiology C: Photochemistry Reviews* **22**, 84–102 (2015).
8. Kao, Y. T. *et al.* Ultrafast dynamics of flavins in five redox states. *Journal of the American Chemical Society* **130**, 13132–13139 (2008).
9. Liu, Z. *et al.* Determining complete electron flow in the cofactor photoreduction of oxidized photolyase. *Proceedings of the National Academy of Sciences* **110**, 12966–12971 (2013).
10. Müller, P., Ignatz, E., Kiontke, S., Brettel, K. & Essen, L. O. Sub-nanosecond tryptophan radical deprotonation mediated by a protein-bound water cluster in class II DNA photolyases. *Chemical Science* **9**, 1200–1212 (2018).
11. Nohr, D. *et al.* Extended Electron-Transfer in Animal Cryptochromes Mediated by a Tetrad of Aromatic Amino Acids. *Biophysical journal* **111**, 301–311 (2016).

12. Aubert, C., Vos, M. H., Mathis, P., Eker, A. P. & Brettel, K. Intraprotein radical transfer during photoactivation of DNA photolyase. *Nature* **405**, 586–590 (2000).

13. Sancar, A. Mechanisms of DNA Repair by Photolyase and Excision Nuclease (Nobel Lecture). *Angewandte Chemie - International Edition* **55**, 8502–8527 (2016).

14. Zhong, D. Electron Transfer Mechanisms of DNA Repair by Photolyase. *Annual Review of Physical Chemistry* **66**, 691–715 (2015).

15. Zhao, X. *et al.* Reaction mechanism of (6-4) photolyase. *Journal of Biological Chemistry* **272**, 32580–32590 (1997).

16. Zhang, M., Wang, L. & Zhong, D. Photolyase: Dynamics and electron-transfer mechanisms of DNA repair. *Archives of Biochemistry and Biophysics* **632**, 158–174 (2017).

17. Chaves, I. *et al.* The Cryptochromes: Blue Light Photoreceptors in Plants and Animals. *Annual Review of Plant Biology* **62**, 335–364 (2011).

18. Sancar, A. & Zhong, D. It is chemistry but not your grandfather's chemistry. *Biochemistry* **56**, 1–2 (2017).

19. Brettel, K. & Byrdin, M. Reaction mechanisms of DNA photolyase. *Current Opinion in Structural Biology* **20**, 693–701 (2010).

20. Müller, F. Flavin radicals: Chemistry and biochemistry. *Free Radical Biology and Medicine* **3**, 215–230 (1987).

21. Balland, V., Byrdin, M., Eker, A. P. M., Ahmad, M. & Brettel, K. What Makes the Difference between a Cryptochrome and DNA Photolyase? A Spectroelectrochemical Comparison of the Flavin Redox Transitions. *Journal of the American Chemical Society* **131**, 426–427 (2009).

22. Park, H., Kim, S., Sancar, A. & Deisenhofer, J. Crystal structure of DNA photolyase from Escherichia coli. *Science* **268**, 1866–1872 (1995).

23. Kiontke, S. *et al.* Crystal structures of an archaeal class II DNA photolyase and its complex with UV-damaged duplex DNA. *The EMBO journal* **30**, 4437–49 (2011).

24. Mees, A. *et al.* Crystal structure of a photolyase bound to a CPD-like DNA lesion after in situ repair. *Science* **306**, 1789–1793 (2004).

25. Kort, R., Komori, H., Adachi, S. I., Miki, K. & Eker, A. DNA apophotolyase from Anacystis nidulans: 1.8 Å structure, 8-HDF reconstitution and X-ray-induced FAD reduction. *Acta Crystallographica Section D: Biological Crystallography* **60**, 1205–1213 (2004).

26. Chapman, H. N. *et al.* Femtosecond X-ray protein nanocrystallography. *Nature* **470**, 73–78 (2011).

27. Neutze, R. & Moffat, K. Time-resolved structural studies at synchrotrons and X-ray free electron lasers: Opportunities and challenges. *Current Opinion in Structural Biology* vol. 22 651–659 (2012).

28. Spence, J. C. H. XFELs for structure and dynamics in biology. *IUCrJ* **4**, 322–339 (2017).

29. Coquelle, N. *et al.* Chromophore twisting in the excited state of a photoswitchable fluorescent protein captured by time-resolved serial femtosecond crystallography. *Nature Chemistry* **10**, 31–37 (2018).

30. Nango, E. *et al.* A three-dimensional movie of structural changes in bacteriorhodopsin. *Science* **354**, 1552–1557 (2016).

31. Nogly, P. *et al.* Retinal isomerization in bacteriorhodopsin captured by a femtosecond x-ray laser. *Science* **361**, (2018).

32. Tenboer, J. *et al.* Time-resolved serial crystallography captures high-resolution intermediates of photoactive yellow protein. *Science* **346**, 1242–1246 (2014).

33. Skopintsev, P. *et al.* Femtosecond-to-millisecond structural changes in a light-driven sodium pump. *Nature* **583**, 314–318 (2020).

34. Kupitz, C. *et al.* Serial time-resolved crystallography of photosystem II using a femtosecond X-ray laser. *Nature* **513**, 261–265 (2014).

35. Pande, K. *et al.* Femtosecond structural dynamics drives the trans/cis isomerization in photoactive yellow protein. *Science (New York, N.Y.)* **352**, 725–9 (2016).

36. Schmidt, M. Time-resolved macromolecular crystallography at pulsed X-ray sources. *International Journal of Molecular Sciences* vol. 20 1401 (2019).

37. Rould, M. A. & Carter, C. W. Isomorphous Difference Methods. *Methods in Enzymology* **374**, 145–163 (2003).

38. Nakai, S., Yoneda, F. & Yamabe, T. Theoretical study on the lowest-frequency mode of the flavin ring. *Theoretical Chemistry Accounts* **103**, 109–116 (1999).

39. Fox, K. M. & Karplus, P. A. Old yellow enzyme at 2 A resolution: overall structure, ligand binding, and comparison with related flavoproteins. *Structure (London, England : 1993)* **2**, 1089–105 (1994).

40. Lennon, B. W., Williams, C. H. & Ludwig, M. L. Crystal structure of reduced thioredoxin reductase from Escherichia coli: Structural flexibility in the isoalloxazine ring of the flavin adenine dinucleotide cofactor. *Protein Science* **8**, 2366–2379 (2008).

41. White, T. A., Johnson, W. H., Whitman, C. P. & Tanner, J. J. Structural basis for the inactivation of Thermus thermophilus proline dehydrogenase by N-propargylglycine. *Biochemistry* **47**, 5573–5580 (2008).

42. Draper, R. D. & Ingraham, L. L. A potentiometric study of the flavin semiquinone equilibrium. *Archives of Biochemistry and Biophysics* **125**, 802–808 (1968).

43. Wijaya, I. M. M., Domratcheva, T., Iwata, T., Getzoff, E. D. & Kandori, H. Single Hydrogen Bond Donation from Flavin N5 to Proximal Asparagine Ensures FAD Reduction in DNA Photolyase. *Journal of the American Chemical Society* **138**, 4368–4376 (2016).

44. Iwata, T., Zhang, Y., Hitomi, K., Getzoff, E. D. & Kandori, H. Key dynamics of conserved asparagine in a cryptochrome/photolyase family protein by Fourier transform infrared spectroscopy. *Biochemistry* **49**, 8882–8891 (2010).

45. Ludwig, M. L., Schopfer, L. M., Metzger, A. L., Pattridge, K. A. & Massey, V. Structure and Oxidation-Reduction Behavior of 1-Deaza-FMN Flavodoxins: Modulation of Redox Potentials in Flavodoxins. *Biochemistry* **29**, 10364–10375 (1990).

46. Walsh, J. D. & Miller, A. F. Flavin reduction potential tuning by substitution and bending. *Journal of Molecular Structure: THEOCHEM* **623**, 185–195 (2003).

47. Domratcheva, T. Neutral histidine and photoinduced electron transfer in DNA photolyases. *Journal of the American Chemical Society* **133**, 18172–18182 (2011).

48. Dereka, B. *et al.* Direct Observation of a Photochemical Alkyne-Allene Reaction and of a Twisted and Rehybridized Intramolecular Charge-Transfer State in a Donor-Acceptor Dyad. *Journal of the American Chemical Society* **139**, 16885–16893 (2017).

49. Kao, Y.-T. *et al.* Ultrafast Dynamics and Anionic Active States of the Flavin Cofactor in Cryptochrome and Photolyase. *Journal of the American Chemical Society* **130**, 7695–7701 (2008).

50. Damiani, M. J., Nostedt, J. J. & O'Neill, M. A. Impact of the N5-proximal Asn on the thermodynamic and kinetic stability of the semiquinone radical in photolyase. *The Journal of biological chemistry* **286**, 4382–91 (2011).

51. Berndt, A. *et al.* A novel photoreaction mechanism for the circadian blue light photoreceptor Drosophila cryptochrome. *Journal of Biological Chemistry* **282**, 13011–13021 (2007).

52. Mowat, C. G. *et al.* Kinetic and crystallographic analysis of the key active site acid base arginine in a soluble fumarate reductase. *Biochemistry* **40**, 12292–12298 (2001).

53. Senger, M. *et al.* How FeFe-Hydrogenase Facilitates Bidirectional Proton Transfer. *Journal of the American Chemical Society* **141**, 17394–17403 (2019).

54. Stevens, D. R. & Hammes-Schiffer, S. Examining the Mechanism of Phosphite Dehydrogenase with Quantum Mechanical/Molecular Mechanical Free Energy Simulations. *Biochemistry* **59**, 943–954 (2020).

55. van der Kamp, M. W., Perruccio, F. & Mulholland, A. J. High-level QM/MM modelling predicts an arginine as the acid in the condensation reaction catalysed by citrate synthase. *Chemical Communications* 1874–1876 (2008) doi:10.1039/b800496j.

56. Keenholtz, R. A. *et al.* Arginine as a general acid catalyst in serine recombinase-mediated DNA cleavage. *Journal of Biological Chemistry* **288**, 29206–29214 (2013).

57. Paddock, M. L. *et al.* ENDOR spectroscopy reveals light induced movement of the H-bond from Ser-L223 upon forming the semiquinone (QB-•) in reaction centers from Rhodobacter sphaeroides. *Biochemistry* **46**, 8234–8243 (2007).

58. Sugahara, M. *et al.* Grease matrix as a versatile carrier of proteins for serial crystallography. *Nature Methods* **12**, 61–63 (2014).

59. Yabashi, M., Tanaka, H. & Ishikawa, T. free-electron lasers Overview of the SACLA facility. *J. Synchrotron Rad* **22**, 477–484 (2015).

60. Nakane, T. *et al.* Data processing pipeline for serial femtosecond crystallography at SACLA. *Journal of Applied Crystallography* **49**, 1035–1041 (2016).

61. White, T. A. *et al. CrystFEL* : a software suite for snapshot serial crystallography. *Journal of Applied Crystallography* **45**, 335–341 (2012).

62. Winn, M. D. *et al.* Overview of the CCP4 suite and current developments. *Acta crystallographica. Section D, Biological crystallography* **67**, 235–42 (2011).

63. Genick, U. K. *et al.* Structure of a Protein Photocycle Intermediate by Millisecond Time-Resolved Crystallography. *Science* **275**, 1471–1475 (1997).

64. Carrillo, M. *et al.* High-resolution Crystal Structures of Transient Intermediates in the Phytochrome Photocycle. *Structure* 2020.09.16.298463 (2021) doi:10.1101/2020.09.16.298463.

65. Claesson, E. *et al.* The primary structural photoresponse of phytochrome proteins captured by a femtosecond x-ray laser. *eLife* **9**, (2020).

66. Afonine, P. v. *et al.* Towards automated crystallographic structure refinement with *phenix.refine*. *Acta Crystallographica Section D Biological Crystallography* **68**, 352–367 (2012).

67. von Stetten, D. *et al. In crystallo* optical spectroscopy (*ic* OS) as a complementary tool on the macromolecular crystallography beamlines of the ESRF. *Acta Crystallographica Section D Biological Crystallography* **71**, 15–26 (2015).

Acknowledgments

The XFEL experiments were performed at the BL2 of SACLA with the approval of the Japan Synchrotron Radiation Research Institute (JASRI) (Proposal No. 2017A8019, 2017B8052, 2018A8008, 2018B8031, 2019A8014, 2019B8005). We would like to thank Tzu-Chun Hsiao, and Miu-lun Wu for their assistance in sample preparation. We are also grateful to Tomoyuki Tanaka, Toshi Arima, Yoshinori Matsuura, Hisashi Naitow, Naoki Kunishima, Tetsukon Kin, and the members of Engineering Support Team of SACLA for help during our X-ray experiments, as well as to Takanori Nakane for his introduction to CrystFEL. We thank all staff members of the TPS05A beamline, NSRRC, a national user facility supported by MOST, ROC, and in particular Chien-Chang Tseng and Chung-Kuang Chou for their help in setting up non-standard conditions for crystal testing. Also, Hui-Lin Shr (Crystallization Facility of the Institute of Biological Chemistry, Academia Sinica) provided the location for crystallization under non-standard conditions, which were initially tested with equipment kindly provided by Dr. Shin-Guang Shyu. We would like to thank Dr. Thomas C. Terwilliger (Los Alamos National Laboratory) for his kind help in understanding the theoretical underpinnings of Bayesian difference refinement. We would also like to thank Guillaume Gotthard for his

assistance in acquiring the redox-dependent *in crystallo* spectra at the ID29S-Cryobench laboratory, which is a platform of the Grenoble Instruct-ERIC center (ISBG; UMS 3518 CNRS-CEA-UGA-EMBL) within the Grenoble Partnership for Structural Biology (PSB). Finally, we would like to thank Mr. Alvaro Maestre Reyna for help in setting up the necessary scripts and macros for calculating extrapolated structure factors.

Funding

The work was supported by Academia Sinica and the Taiwan Protein Project funded by MOST (Grant No. AS-KPQ-105-TPP and AS-KPQ-109-TPP2), and in part by JSPS KAKENHI (16K01942). L.O.E. thanks for support by Air Force Office of Scientific Research (AFOSR; Grant No. FA9550-14-1-0409) and German Research Foundation (DFG, Grant No. ES152/18). S.I. acknowledges support by Platform Project for Supporting Drug Discovery and Life Science Research (Basis for Supporting Innovative Drug Discovery and Life Science Research (BINDS)) from Japan Agency for Medical Research and Development (AMED).

Author contributions

MMR, SI, LOE, YB, and MDT conceived the research and designed experiments. MMR, CHY, EN, WCH, EPGNP, WJW, PHW, SFB, MS, HJE, HYW, CCL, KFH, YKC, JHL, JHW, WG, CWC, AHP, MS, SO, YH, AY, RT, TT, LF, KT, RS, AR, JY, LOE, and YB performed experiments. MMR, CHY, EN, YJ, SK, IS, LOE, YB, and MDT analyzed the data. MMR, EPGNP, LOE, and AR performed *in-crystallo* spectroscopy. MMR and CHY established and analyzed the multiple refinement approach protocol. KCH performed structure-based PDB search. MMR, WJW, CHY, AR, LOE, YB, and MDT wrote the manuscript.

Additional information

Supplementary information is available in the online version of the paper. Correspondence and requests for materials should be addressed to Ming-Daw Tsai. Structural models, along with structure factors presented here can be found under PDB accession codes 7F8T, 6LT3, 6LT1, 6LT2, 6LM4, 6LMB, 6LM5, 6LM6, 6LM7, 6LM8, 6LMC, 6LM9, 6LME, 6LMA,7CLW, 7C3P, 7C3R, 7C3W, 7C3X, 7CLM, 7CLN, 7CLO, 7CLP, and 7CLQ.

Competing financial interests

The authors declare no conflict of financial interest.